Promoted Multimetal Oxide Catalysts for the Generation of Hydrogen via Ammonia Decomposition

Han Yan,[†] Yue-Jiao Xu,[†] Ying-Qiu Gu,[†] Hao Li,[†] Xu Wang,[‡] Zhao Jin,*[†] Shuo Shi,[§] Rui Si,*[‡] Chun-Jiang Jia,*[†] and Chun-Hua Yan[§]

[†]Key Laboratory for Colloid and Interface Chemistry, Key Laboratory of Special Aggregated Materials, School of Chemistry and Chemical Engineering, Shandong University, Jinan 250100, China

[‡]Shanghai Synchrotron Radiation Facility, Shanghai Institute of Applied Physics, Chinese Academy of Sciences, Shanghai 201204, China

[§]Beijing National Laboratory for Molecular Sciences, State Key Lab of Rare Earth Materials Chemistry and Applications, PKU-HKU Joint Lab in Rare Earth Materials and Bioinorganic Chemistry, Peking University, Beijing 100871, China

S *Supporting Information*

ABSTRACT: Mesoporous multimetal oxide microspheres (Ni−Ce−Al−O) with tuned and uniformly distributed composition are prepared through an aerosol-assisted self-assembly approach and further used as catalysts for ammonia decomposition. The as-prepared and spent materials are characterized by various techniques including *ex situ/in situ* X-ray diffraction (XRD), X-ray absorption fine structure (XAFS), scanning electron microscope (SEM)/transmission electron microscope (TEM), X-ray photoelectron spectroscopy (XPS), and N_2-adsorption. The tricomponent Ni−Ce−Al−O catalysts show great superiority over pure NiO or bicomponent catalysts (Ni−Ce−O and Ni−Al−O) in both catalytic activity and durability. By using H_2-TPR combined with *in situ* XRD, we have identified metallic Ni^0 as the active crystalline phase and further confirmed the strong interaction between alumina and other components. This strong interaction helps suppress the growth of both metallic Ni^0 as active site and ceria as promoter under the harsh catalytic conditions (high temperature and reducing atmosphere) and thus improves the activity and stability simultaneously.
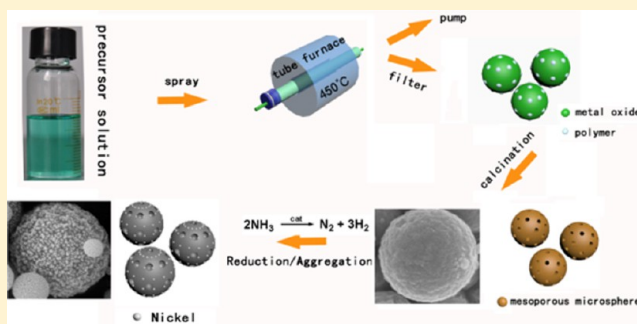
INTRODUCTION

Mesoporous metal oxide materials (MMOMs) with size ranging from nanometers to micrometers have aroused increasing attention because of their compositional flexibility, high surface area, and connected pore networks. Due to these unique properties, MMOMs have been applied to a host of fields, including catalysis,[1−5] dye adsorption,[6−8] imaging, and drug delivery.[9−13] Among MMOMs, mesoporous transition metal oxides exhibit particular importance in catalysis because of their unique redox properties.

Previous synthetic tactics of MMOMs mostly involved time-consuming methods like the sol−gel method[14] or intricate methods like the hard-template method.[15,16] By contrast, the aerosol-assisted self-assembly approach (AASA),[17,18] a combination of aerosol-spray and evaporation-induced self-assembly, is an efficient and promising strategy. The aerosol-spray technique is a suitable method that is capable of simple, large-scale, and continuous production of nanoparticles. The evaporation-induced self-assembly process provides yielded MMOMs with spherical morphology and high surface area.[19] The whole AASA approach requires the employ of block copolymer, which serves as a soft template and is removed after

self-assembly. Using the AASA method, various MMOMs have been prepared and applied in many fields such as drug release,[20] luminescence emitting,[21] photocatalysis,[22] pollutant disposal,[23,24] and electrocatalysis.[25] Recently, the universality of synthesizing mesoporous metal oxides from metal nitrates has been reported.[26] However, most of the previously prepared MMOMs via the AASA approach are monocomponent metal oxides. The reports of multicomponent MMOMs produced via AASA are still not extensive, and the underlying interaction between different components, which may have a great influence on the structure and performance of the materials, has not been well studied.

Ammonia is an outstanding hydrogen source for fuel cell applications[27,28] since the decomposition of ammonia generates high purity hydrogen gas without CO_x. It is well-known that the fused iron catalysts with small amounts of promoters (Al_2O_3, CaO, and K_2O) have been industrially used in ammonia synthesis for decades.[29,30] However, due to the different

binding energies for ammonia synthesis and decomposition, which result from the different reaction conditions,[31] the fused iron catalysts have rarely been applied to ammonia decomposition.[32] The supported metal or metal oxides catalysts, by contrast, have been studied intensively. According to previous studies, many noble metals (Ru,[33−35] Rh,[36,37] Ir[38,39]) and transition metals or their oxides (Fe,[40−42] Mo,[35,43] Co,[41,42,44] Ni[45−50]) have been used as catalysts for ammonia decomposition. In consideration of the high cost and limited availability of noble metals, transition metal catalysts are promising alternatives and have been widely investigated due to their good performance and low cost.[40,46] However, most of the transition metal catalysts prepared by traditional synthetic methods such as coprecipitation[45,46] and the deposition−precipitation method[47] suffer from the poor stability caused by the sintering of active species. To resolve this problem, many synthetic strategies have been developed to prepare stable catalysts against sintering at high temperatures. For example, catalysts of iron oxide nanoparticles embedded in the channels of mesoporous carbon material (CMK-5) or in porous silica shell were synthesized.[51] These catalysts showed stable performance during the catalytic tests for ammonia decomposition. However, the synthesis procedure of the embedded/encapsulated catalysts is normally complicated. Also the activities of these catalysts cannot be fully optimized due to the ineffective interaction between the active transition metal species and the support materials, which is caused by the limited loadings of transition metals and the small contact interface of different compositions. Thus, applying an effective synthetic way to fabricate transition metal composite catalysts in which different components interact effectively based on their homogeneous dispersion is very likely to benefit the exploration of highly efficient and stable catalysts for the production of hydrogen via ammonia decomposition.

Among the various transition metal catalysts for ammonia decomposition, nickel-based catalysts have been extensively studied.[45−50] Current studies on nickel-based catalysts are mostly supported catalysts in which alumina (Al_2O_3) is commonly used as support due to its great thermal stability;[45,48] meanwhile, rare earth oxides such as ceria (CeO_2) are also used as cocatalysts to enhance the catalytic activity.[48,52] Although considerable efforts have been directed, the controllable synthesis and structure−property relationship for nickel catalysts are still to be developed and explored in depth. Herein, we report a facile and continuous aerosol-assisted self-assembly approach to fabricate mesoporous nickel-based multimetal oxide microspheres with tuned and homogeneously dispersed composition. These as-prepared materials were used as catalysts for the production of hydrogen via ammonia decomposition. Compared with NiO and bimetal oxides of Ni−Ce−O or Ni−Al−O materials, the trimetal system of Ni−Ce−Al−O showed great superiority in both reactivity and stability as catalysts for ammonia decomposition. Systematic investigations demonstrate that the presence of Al_2O_3 greatly improves the dispersion of both nickel oxide and CeO_2, which induced strong interactions between Al_2O_3 with nickel oxide as well as CeO_2. This strong interaction in the Ni−Ce−Al−O system helps suppress the sintering of both the active site (metallic Ni^0) and cocatalyst (CeO_2) under the harsh catalytic conditions and thus improves the activity and stability simultaneously.

■ EXPERIMENTAL SECTION

Materials. All materials were purchased from commercial vendors and used without further modification and purification. Ammonium carbonate (($NH_4)_2CO_3$, 99.0%), nickel nitrate ($Ni(NO_3)_2 \cdot 6H_2O$, 98.0%), cerium nitrate ($Ce(NO_3)_3 \cdot 6H_2O$, 99.5%), and aluminum nitrate ($Al(NO_3)_3 \cdot 9H_2O$, 99.0%) were purchased from Tianjin Kermal Chemical Reagent Factory. The triblock copolymer, (ethylene oxide)$_{106}$-(propylene oxide)$_{70}$-(ethylene oxide)$_{106}$ (F127, M_w = 12 000 g·mol^{-1}), was purchased from Sigma-Aldrich.

Catalyst Synthesis. The preparation of mesoporous oxide microspheres was accomplished using an ultrasonic spray method schematically illustrated in Scheme 1. In order to

Scheme 1. Illustration of the Productive Process in the Aerosol-Assisted Self-Assembly Approach (AASA) for Mesoporous Metal Oxide Microspheres
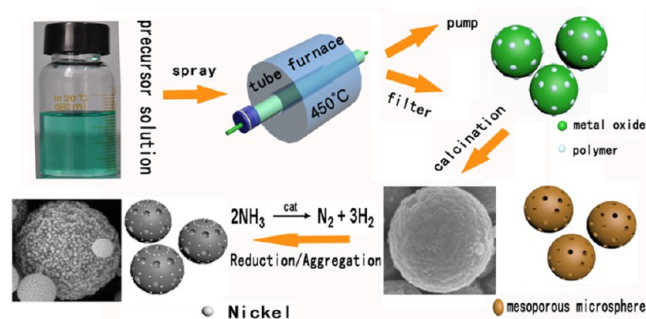
generate the oxide microspheres, Ni $(NO_3)_3 \cdot 6H_2O$, $Ce(NO_3)_3 \cdot 6H_2O$, and $Al(NO_3)_3 \cdot 9H_2O$ (2 mmol in total with certain molar ratio), and triblock copolymer F127 (0.2 g) were dissolved in absolute ethanol (30 mL) to form the precursor solution. The mixture was sonicated for 10 min and then transferred into a household ultrasonic humidifier (1.5 MHz, 30 W). The precursor solution turned into spray after atomization, and the generated spray was carried into a tube furnace (preheated to 450 °C) by N_2. The resultant powder was collected on a piece of filter paper. While in the furnace, the metal salts in the mist drops went through solidification, decomposition, and assisted assembly and finally yielded metal oxide microspheres with inlaid block copolymer F127. The collected powders were stored in a drying oven (80 °C) for 2 h and later calcined at 450 °C in the tube furnace for another 4 h. The calcination was carried out in air atmosphere, and the heating rate was set as 1 °C·min^{-1}. After calcination, the catalysts were crystallized, and F127 was removed. Then the mesoporous structure of the materials was formed. During the following catalytic process, due to the reduction by generated H_2, metallic Ni^0 particles were formed separately out of the surface of the catalysts. The porosity of catalysts was also changed after catalysis. The synthesized catalysts were designated as $Ni_aCe_bAl_cO_x$. The name of each replica is decided by the molar ratio of metal elements. For example, $Ni_{0.5}Ce_{0.1}Al_{0.4}O_x$ means the molar ratio of Ni:Ce:Al is 5:1:4.

The compared catalysts were prepared by a coprecipitation (cp) method by a previously reported procedure.[48] Metal nitrates ($Ni(NO_3)_3 \cdot 6H_2O$, $Ce(NO_3)_3 \cdot 6H_2O$, and $Al(NO_3)_3 \cdot 9H_2O$) and ($NH_4)_2CO_3$ were starting materials. The synthesized catalysts were designated as $Ni_aCe_bAl_cO_x$ cp.

Catalyst Characterization. The *ex-situ* X-ray diffraction (XRD) was carried out on a PANalytical B.V. X'pert3 powder

diffractometer (40 kV, 40 mA), using Cu K_α radiation (λ = 0.15406 nm). The catalyst powder (about 30 mg) was placed on a glass sample holder after grinding. Data were collected by a PIXcel1^D detector in the 10−90° 2θ range with an acquisition time of 8.5 min. The *in-situ* XRD patterns were obtained from the same diffractometer (40 kV, 40 mA, CuK$_\alpha$: λ = 0.15406 nm) by using an Anton Paar XRK900 reaction chamber. About 100 mg of replicas was loaded on a ceramic sample holder (diameter = 10 mm, depth = 1 mm) and then heated from room temperature to 700 °C in a 5% H$_2$/Ar gas mixture. The flow rate of the gas through the replica was set as 30 mL·min^{-1}, and the heating rate was 30 °C·min^{-1}. The XRD patterns were collected at room temperature, 400 °C, 500 °C, 600 °C, and 700 °C, respectively. For each selected temperature, 3 rounds of measurements with each one lasting for 20 min were carried out, and the last round was chosen to analyze the crystallinity.

The X-ray absorption fine structure (XAFS) spectra at the Ni K-edge (E_0 = 8333 eV) were performed at the 20-ID-B beamline of Advanced Photon Source (APS) at 7 GeV and 100 mA or BL14W1 beamline of Shanghai Synchrotron Radiation Facility (SSRF) at 3.5 GeV and 240 mA under "top-up" mode. The XAFS data were recorded under transmission mode with ion chambers for all the powder samples. The energy was calibrated according to the absorption edge of pure Ni foil. Athena and Artemis codes were used to extract the data and fit the profiles. For the X-ray absorption near-edge structure (XANES) part, the experimental absorption coefficients as a function of energies $\mu(E)$ were processed by background subtraction and normalization procedures and reported as "normalized absorption". For the extended X-ray absorption fine structure (EXAFS) part, the Fourier transformed (FT) data in R space were analyzed by the NiO or NiO/Ni model for the Ni−O or Ni−Ni shell, respectively. The passive electron factors, S_0^2, were determined by fitting the experimental Ni foil data and fixing the Ni−Ni coordination number (CN) to be 12 and then fixed for further analysis of the measured samples. The parameters describing the electronic properties (e.g., correction to the photoelectron energy origin, E_0) and local structure environment including CN, bond distance (R), and Debye−Waller (D.W.) factor around the absorbing atoms were allowed to vary during the fit process.

All images of the transmission electron microscope (TEM) were obtained on a JEOL JEM-2100 microscope (200 kV). The scanning electron microscope (SEM) images of replicas before catalytic process were taken on a Hitachi S-4800 ultrahigh-resolution scanning microscope with an acceleration voltage of 5.0 kV. The element mapping results based on the energy-dispersive X-ray spectroscopy (EDS), as well as the SEM images of all magnetic replicas (replicas after catalytic process), were derived from a Zeiss SUPRA 55 scanning microscope with an acceleration voltage of 5.0 kV.

X-ray photoelectron spectroscopy (XPS) analysis was operated on an Axis Ultra analyzer from KratisAnalytica Ltd.

The nitrogen sorption measurements were operated in a Builder SSA-4200 surface area analyzer at 77 K after degassing process at 200 °C for 6 h under vacuum. Pore size distribution of each replica was calculated by applying the Barrett−Joyner−Halenda (BJH) method. Surface area of each replica was calculated by using the Brunauer−Emmett−Teller (BET) method.

Temperature-programmed reduction by hydrogen (H$_2$-TPR) was operated in a Builder PCSA-1000 adsorption instrument which was equipped with a thermal conductivity detector (TCD). An amount of 30 mg of catalysts was loaded in the quartz tube and then heated from room temperature to 1000 °C with a ramping rate of 5 °C min^{-1}. The reduction progress was in a 5% H$_2$/Ar gas mixture at a flow rate of 30 mL min^{-1}. Each sample went through a degassing pretreatment in pure O$_2$ at 300 °C for 30 min before measurement.

Catalytic Tests. For a typical NH$_3$ decomposition experiment, 50 mg (20−40 mesh) of the catalyst was loaded in a quartz tube (inner diameter = 6 mm) fixed bed reactor, and pure gaseous NH$_3$ was passed through the catalyst bed. For the temperature-dependent conversion measurements of NH$_3$, the reactor temperature was increased from 400 to 600 °C in 50 °C steps. At each step, the reaction was allowed to equilibrate for 60 min to reach the steady-state conditions, and data obtained from the last gas chromatography (GC) run at each temperature were used to calculate the conversion value. The catalytic activity of each sample was tested twice, and the first round of tests served as a self-activation process. Blank tests with an empty reaction chamber yielded less than 1% conversion at 600 °C and 10% conversion at 700 °C. The space velocity was set as 18 000 cm^3 g^{-1} h^{-1} for catalytic activity tests. In order to evaluate the stability of the catalyst, the reaction temperature was maintained at 600 °C for more than 45 h, and the catalytic activity was recorded continuously. The space velocity for stability tests was set as 18 000 cm^3 g^{-1} h^{-1} and 90 000 cm^3 g^{-1} h^{-1}, respectively. The apparent activation energy for NH$_3$ decomposition was determined at 380−460 °C, and an equal conversion of 12.5% was controlled by changing temperature and flow rate. The space velocity was varied between 9000 and 60 000 cm^3 g^{-1} h^{-1} by tuning the ammonia flow rates. The concentrations of outlet gases (N$_2$ and NH$_3$) were analyzed by an online GC (Ouhua GC 9160), which is equipped with a thermal conductivity detector (TCD) and Porapark Q column (1.5 m of length).

■ RESULTS AND DISCUSSION

Figure 1 exhibits the scanning electron microscope (SEM) and transmission electron microscope (TEM) images of three representative MMOMs from AASA. The diameters of the microspheres in all replicas range from 0.1 to 2 μm, which is coherent with the size distribution of the mist drop generated in the ultrasonic humidifier.[22] As shown in Figure 1a, 1c, and 1e, the multicomponent products including the Ni−Ce−O, Ni−Al−O, and Ni−Ce−Al−O systems all give morphology of solid microspheres with relatively smooth surfaces, while for pure NiO products (Figure S1a), the microspheres are shrivelled. The collapse of NiO microspheres may be attributed to the poor diffusion ability of Ni^{2+} during the decomposition process of metal nitrates in the furnace.[26,53] The size of NiO nanocrystals forming the microspheres is relatively large (Figure S1b), and the complete self-assembly of pure NiO nanoparticles during the short-time solidification may be more difficult compared with CeO$_2$ microspheres (Figures S1c and S1d) and other multicomponent products. The TEM images of the three samples illustrate that the mesoporous structure of the catalysts is formed in the frameworks.

The X-ray diffraction (XRD) technique is used to investigate the phase and crystallinity of the MMOMs. The XRD patterns in Figure 2a show that it is rhombohedral nickel oxide and cubic cerianite ceria that crystallize in the pore walls of the mesoporous microspheres, respectively. However, no crystalline phases of Al$_2$O$_3$ are determined in all replicas containing Al, suggesting the Al$_2$O$_3$ in the products is completely amorphous.
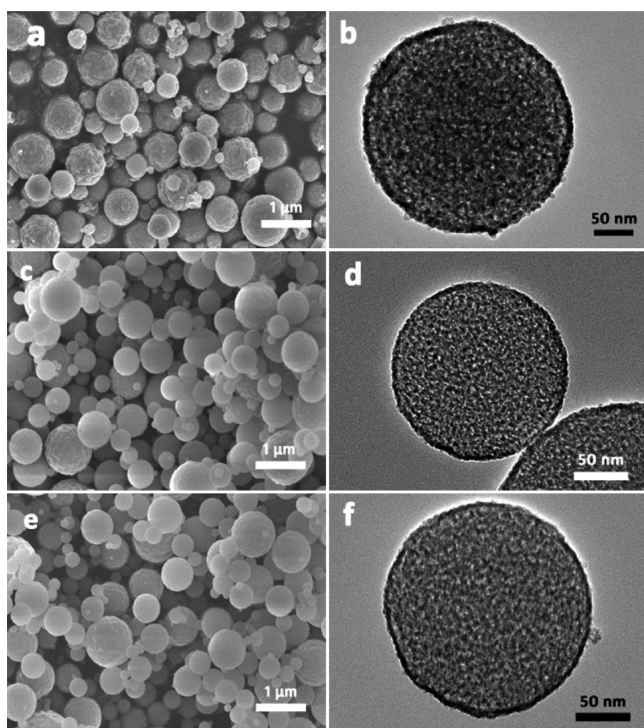
Figure 1. SEM (a, c, e) and TEM (b, d, f) images of typical metal oxide microspheres produced via AASA: (a, b) $Ni_{0.5}Ce_{0.5}O_x$; (c, d) $Ni_{0.5}Al_{0.5}O_x$; and (e, f) $Ni_{0.5}Ce_{0.1}Al_{0.4}O_x$.

Table 1 shows structure parameters including crystalline domain size and surface area of the four replicas. The crystalline domain size of nickel oxide was 15.9 nm, 5.4 nm, 4.6 nm, and 3.6 nm for pure NiO, $Ni_{0.5}Ce_{0.5}O_x$, $Ni_{0.5}Al_{0.5}O_x$, and $Ni_{0.5}Ce_{0.1}Al_{0.4}O_x$, respectively, based on the calculation using the Scherrer equation. The domain size of nickel oxide was apparently smaller after the introduction of ceria and alumina components, which corresponds well to our observation on TEM images (Figure 1b, 1d, and 1f, Figure S1b), indicating that the addition of either Ce or Al improves the dispersion of nickel oxide.

The results of nitrogen adsorption measurements are given in Figure 3. Generally, all multimetal oxide replicas have large Brunauer−Emmett−Teller (BET) surface areas around 100 m^2 g^{-1}. The sorption isotherms and pore-size distribution of the pure NiO sample (Figure 3d) suggest that this material has no porous structures, while isotherms for the other three samples in Figure 3a−c show a defined hysteresis loop and regular pore-

size distribution, which confirms the existence of mesoporous structure. As shown in Figures 3d and S2, the difference in surface areas between NiO (25 m^2 g^{-1}) and CeO$_2$ (120 m^2 g^{-1}) is tremendous, and the TEM and SEM images of pure CeO$_2$ products (Figure S1c and S1d) gave morphology of solid and smooth microspheres. These observations denote that CeO$_2$ nanocrystals serve as the skeleton for the Ni−Ce−O microspheres, and the larger surface area of $Ni_{0.5}Ce_{0.5}O_x$ (152 m^2 g^{-1}) further proves the improvement of nickel oxide dispersion by CeO$_2$. The $Ni_{0.5}Ce_{0.5}O_x$ replica has a well-shaped and pronounced hysteresis loop with a forced closure at a relative pressure of 0.6 because of capillary criticality. In comparison, the $Ni_{0.5}Al_{0.5}O_x$ replica has an apparent adsorption step at about 0.46 P/P$_0$ with a less well-shaped hysteresis loop. The sorption isotherms and pore-size distribution both suggest that the mesoporous structure of $Ni_{0.5}Ce_{0.5}O_x$ comes from the addition of ceria. Besides, the $Ni_{0.5}Al_{0.5}O_x$ replica has a fraction of larger mesopores between 20 and 40 nm. The occurrence of large mesopores may arise from the tiny amorphous Al$_2$O$_3$ particles and partial hollow structures inside the spheres, which can as well explain the higher BET surface area of this replica. The $Ni_{0.5}Ce_{0.1}Al_{0.4}O_x$ replica has larger mesopores than the other replicas, but the surface area is not as large as the one of $Ni_{0.5}Al_{0.5}O_x$. Considering the observation in Figure 1c and d, such a decrease in surface area might be attributed to the destruction of mesoporosity during the crystallization of CeO$_2$.

The surface structure of Ni−Ce−O and Ni−Ce−Al−O replicas was investigated using X-ray photoelectron spectroscopy (XPS), the results of which are illustrated in Figure 4. In Figure 4a, the Ni 2p1/2 peak at 872.9 eV and the corresponding satellite peak at 882.2 eV[54] are evidently detectable on both replicas. Besides, the high intensity of the Ni 2p3/2 peak at 853.7 eV with a shakeup satellite peak at 860.9 eV[54] suggests the presence of NiO or Ni^{2+}. After a temperature-dependent catalytic test, as shown in Figure 4b, the Ni 2p1/2 peak at 872.9 eV and the corresponding satellite peak at 882.2 eV[54] are still detectable, while a characteristic peak of Ni(0) appears at 852.6 eV[54,55] instead of the Ni^{2+} characteristic peaks for both replicas. The XPS results of Ni 2p prove that NiO on the surface of catalysts is reduced to metallic Ni^0 by generated H$_2$ during a temperature-dependent catalytic test, and this evidence is consistent with the ex-situ XRD data in Figure 2b. Meanwhile, despite the slight difference in intensity, the Ce 3d characteristic peaks of the two replicas (Figure 4c and 4d) correspond well to the ones of oxidized CeO$_2$.[56] The Ce 3d characteristic peaks remain unchanged after a temper-
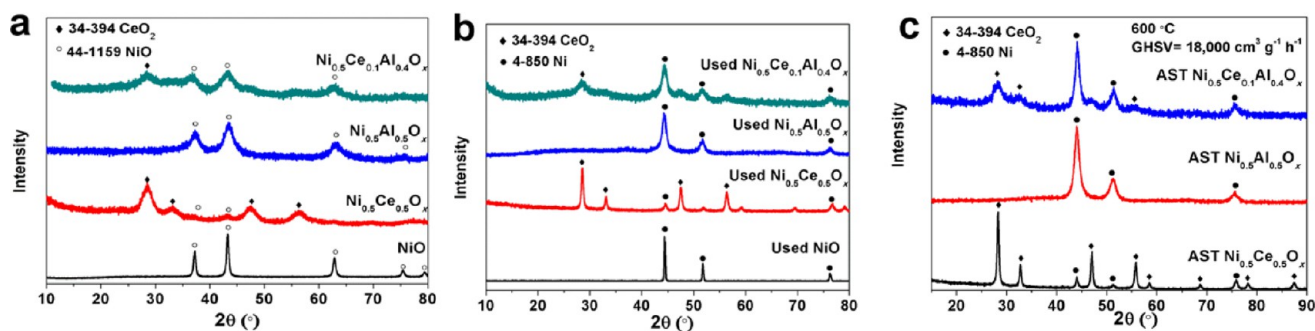
Figure 2. X-ray diffraction (XRD) patterns of (a) typical fresh replicas produced via AASA; (b) replicas after temperature-dependent catalytic tests (used replicas); and (c) replicas after stability test (AST replicas) at 600 °C (GHSV = 18 000 cm^3 g^{-1} h^{-1}).

Table 1. Physical Properties of Typical Fresh and Used Replicas

sample (fresh)	surface area/m^2 g^{-1}	d_{NiO}/nm[a]	sample (used)	surface area/m^2 g^{-1}	d_{Ni}/nm[a]
NiO	25	15.9	NiO	-	33.1
Ni$_{0.5}$Ce$_{0.5}$O$_x$	152	5.4	Ni$_{0.5}$Ce$_{0.5}$O$_x$	34	16.5
Ni$_{0.5}$Al$_{0.5}$O$_x$	278	4.6	Ni$_{0.5}$Al$_{0.5}$O$_x$	175	8.9
Ni$_{0.5}$Ce$_{0.1}$Al$_{0.4}$O$_x$	149	3.6	Ni$_{0.5}$Ce$_{0.1}$Al$_{0.4}$O$_x$	106	7.6

[a]Calculated from XRD patterns using the Scherrer equation.
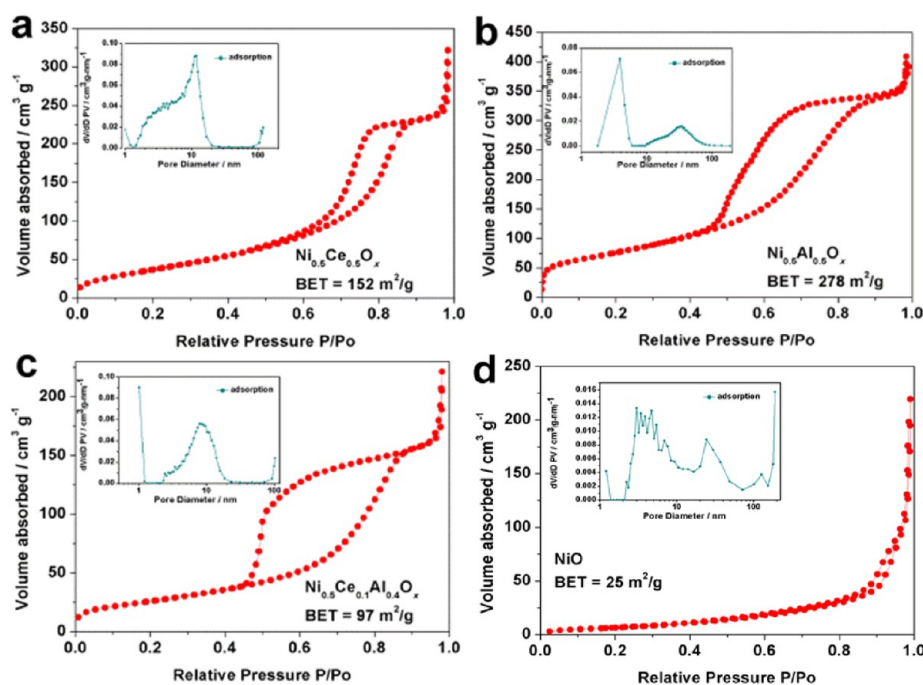
Figure 3. Nitrogen sorption isotherms of representative replicas produced via AASA: (a) Ni$_{0.5}$Ce$_{0.5}$O$_x$; (b) Ni$_{0.5}$Al$_{0.5}$O$_x$; (c) Ni$_{0.5}$Ce$_{0.1}$Al$_{0.4}$O$_x$; and (d) NiO. The respective Barrett–Joyner–Halenda (BJH) pore size distributions are shown in the inset figures.
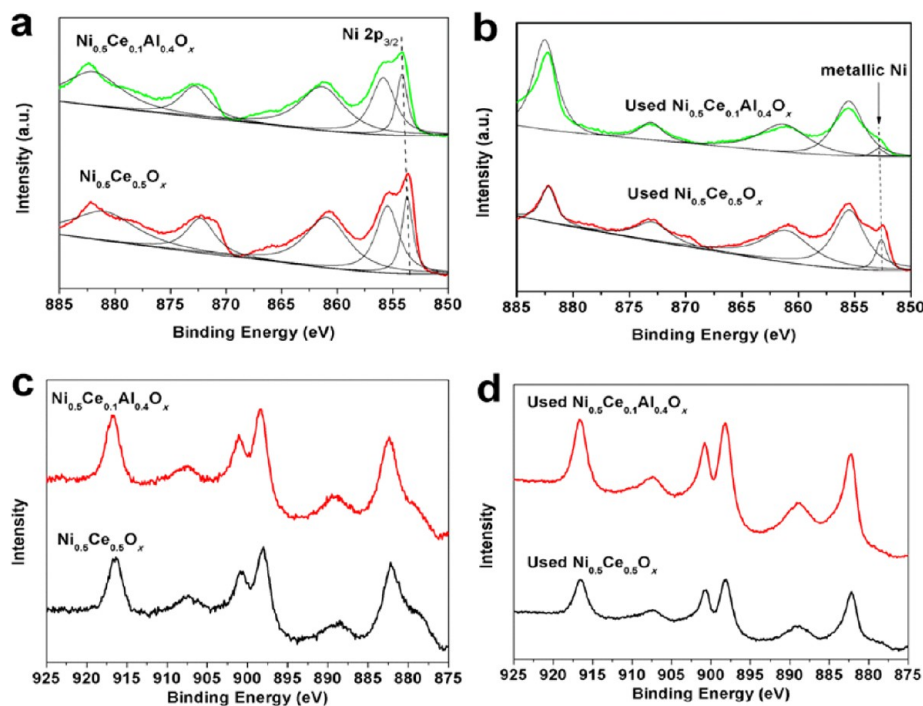

Figure 4. XPS spectra of the Ni–Ce–O and Ni–Ce–Al–O replicas: (a) Ni 2p spectra for fresh sample; (b) Ni 2p spectra used samples after temperature-dependent catalysis test; (c) Ce 3d spectra for fresh replicas; and (d) Ce 3d for replicas after temperature-dependent catalytic test.
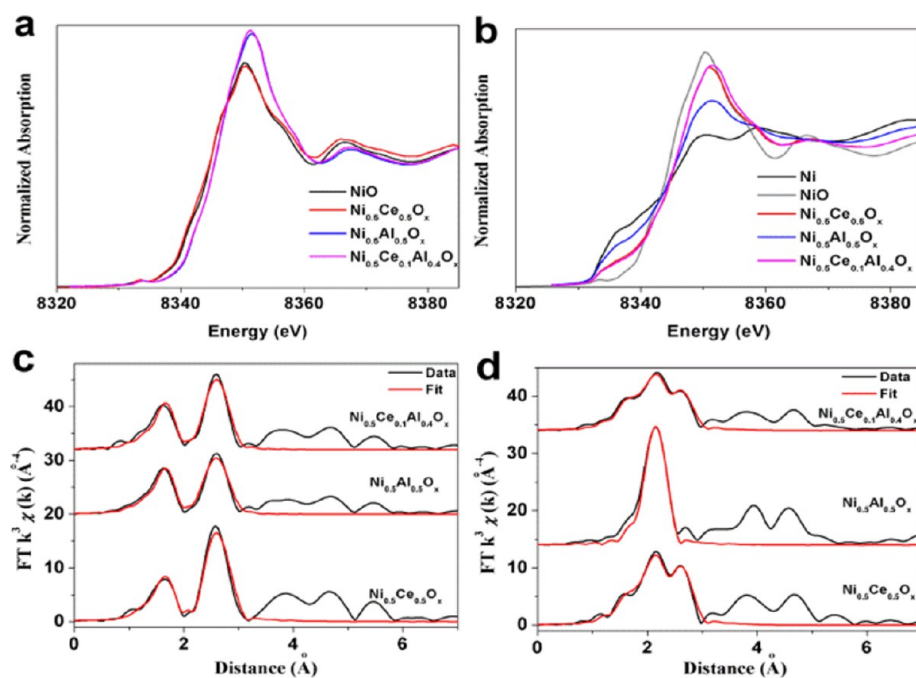
Figure 5. XAFS of fresh (a, c) and used (b, d) representative samples: (a, b) XANES; (c, d) EXAFS.

Table 2. EXAFS Fitting Results (R: Distance; CN: Coordination Number) on Ni−O and Ni−Ni Shells of the Ni-Based Catalysts

sample	Ni−O		Ni−Ni	
	R [Å]	CN	R [Å]	CN
Ni foil[a]	—	—	2.492	12
NiO[a]	2.084	6	2.947	12
$Ni_{0.5}Ce_{0.5}O_x$ (fresh)	2.08 ± 0.02	6	2.96 ± 0.01	12
$Ni_{0.5}Al_{0.5}O_x$ (fresh)	2.07 ± 0.01		2.97 ± 0.01	
$Ni_{0.5}Ce_{0.1}Al_{0.4}O_x$ (fresh)	2.07 ± 0.01		2.96 ± 0.01	
$Ni_{0.5}Ce_{0.5}O_x$ (used)	2.08 ± 0.04	3.7 ± 1.4	2.48 ± 0.02	4.2 ± 1.2
			2.95 ± 0.02	6.0 ± 1.9
$Ni_{0.5}Al_{0.5}O_x$ (used)	—	—	2.49 ± 0.01	7.6 ± 0.9
$Ni_{0.5}Ce_{0.1}Al_{0.4}O_x$ (used)	2.07 ± 0.03	1.3 ± 0.6	2.48 ± 0.02	3.5 ± 0.8
			2.95 ± 0.02	4.1 ± 1.1

[a]Calculated from the Ni or NiO structural model.

ature-dependent catalytic test, indicating CeO_2 maintains the valence of +4 during the catalytic process in all catalysts.

The investigations using XRD and XPS give the general structural information for the Ni-based catalysts; however, the local structure around the measured Ni atoms, which is very important to identify the catalytically active site, was missing. Here, X-ray absorption fine structure (XAFS) technique was used to investigate the structure in the Ni-based catalysts with different components, which is elementally sensitive and very powerful to determine the electronic and local structure of metals. In the X-ray absorption near edge structure (XANES) region (Figure 5a), the edge energy, the white line intensity, and the pre-edge features are clearly related to the oxidation state of Ni(II) (NiO as reference) for all the fresh samples, which is consistent with the XPS results (Figure 4). Meanwhile, the extended X-ray absorption fine structure (EXAFS) fitting results in Figure 5c and Table 2 confirm the identical local structure as bulk NiO for the Ni−Ce−Al−O catalysts before the catalytic tests for the ammonia decomposition reaction, i.e., first shell of Ni−O at 2.07−2.08 Å with CN = 6 and second shell of Ni−Ni at 2.96−2.97 Å with CN = 12.

The catalytic performance of the Ni-based mesoporous microspheres for the production of hydrogen from the decomposition of ammonia was investigated in detail. We used Ni−Ce−O, Ni−Al−O, and Ni−Ce−Al−O systems as catalysts of ammonia decomposition, with the pure NiO sample as reference catalyst. In order to optimize the catalytic properties of the Ni−Ce−O, Ni−Al−O, and Ni−Ce−Al−O catalysts, replicas with different Ni/M (M = Ce or Al) ratios were synthesized and tested. Among all the synthesized catalysts, the replica of $Ni_{0.5}Ce_{0.5}O_x$ and $Ni_{0.5}Al_{0.5}O_x$ with the highest ammonia conversion was chosen as typical examples from Ni−Ce−O and Ni−Al−O systems (Figure S3a and S3b). For Ni−Ce−Al−O catalysts, the Ce/Al ratio is tuned, and the molar ratio of Ni is fixed at 50% of all metal elements. All Ni−Ce−Al−O catalysts with different Ce/Al ratios give nearly the same NH_3 conversion (Figure S3c), suggesting the Ce/Al ratio in the Ni−Ce−Al−O system does not have a straight impact on catalytic activity.

Generally speaking, the size of the metallic Ni^0 domain has a straight relationship to the activity of the catalysts. The smaller the Ni^0 domain is, the higher activity the catalyst may reach.
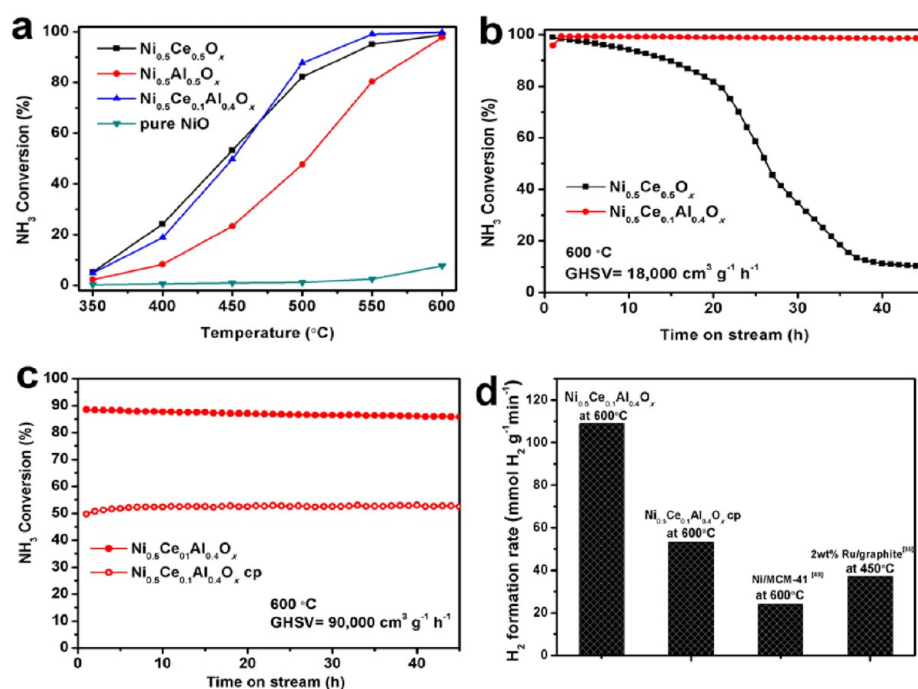
Figure 6. (a) Catalytic activities of three representative replicas of mono-, bi-, and trimetal oxide catalysts. (b) Stability tests of the representative replicas at 600 °C (GHSV = 18 000 cm^3 g^{-1} h^{-1}). (c) Stability tests of the representative replicas at 600 °C (GHSV = 90 000 cm^3 g^{-1} h^{-1}). (d) Hydrogen formation rate of $Ni_{0.5}Ce_{0.1}Al_{0.4}O_x$ and $Ni_{0.5}Ce_{0.1}Al_{0.4}O_x$ cp during stability test (the data from the end of tests at 45 h, 600 °C, GHSV = 90 000 cm^3 g^{-1} h^{-1}) and of Ni/MCM-41 catalyst[49] and 2 wt % Ru/graphite catalyst.[35]

This tendency is coherent with previous results from ultraviolet photoelectron spectrometer (UPS)/XPS investigation,[57,58] which suggests a pronounced structure sensitivity of Ni^0 for ammonia decomposition. The low NH$_3$ conversion (about 8% at 600 °C) (Figure 6a) and the large crystalline domain size (15.9 nm, Table 1) of a pure NiO replica further prove this tendency. For common promoters of nickel-based catalyst for ammonia decomposition, cerium is known to have a better performance on the enhancement of activity over aluminum;[59,60] however, the impacts of promoter and support are to be explored in the Ni−Ce−Al−O composite system. As illustrated in Figure 6a, the NH$_3$ conversion of the $Ni_{0.5}Ce_{0.5}O_x$ replica is obviously higher than that of $Ni_{0.5}Al_{0.5}O_x$ at 350−550 °C, so the Ni−Al−O system is not an excellent catalyst for ammonia decomposition compared to the Ni−Ce−O with respect to catalytic activity. However, during the long-term stability test, the NH$_3$ conversion of $Ni_{0.5}Ce_{0.5}O_x$ plummeted from 100% to 10% within 45 h at 600 °C, undergoing an obvious deactivation process (Figure 6b), which suggests that the $Ni_{0.5}Ce_{0.5}O_x$ catalyst was unstable under this reaction condition. By contrast, though the catalytic activity is relatively lower, $Ni_{0.5}Al_{0.5}O_x$ exhibited better stability under 600 °C during the long-term tests (Figure S4).

Based on former results, we further developed a Ni−Ce−Al−O system, aiming to keep the high catalytic activity and boost the stability. Knowing that Al is much cheaper than Ce, replicas with the lowest ($Ni_{0.5}Ce_{0.1}Al_{0.4}O_x$) Ce/Al ratio were chosen as typical catalysts for further investigations. The catalytic activity of the $Ni_{0.5}Ce_{0.1}Al_{0.4}O_x$ catalyst is similar to that of $Ni_{0.5}Ce_{0.5}O_x$ (Figure 6a), and the $Ni_{0.5}Ce_{0.1}Al_{0.4}O_x$ catalyst shows great stability under 600 °C during the long-term tests compared with the $Ni_{0.5}Ce_{0.5}O_x$ sample (Figure 6b). The $Ni_{0.5}Ce_{0.1}Al_{0.4}O_x$ catalyst exhibited the same excellent stability with $Ni_{0.5}Al_{0.5}O_x$ at a very high space velocity of 90 000 cm^3 g^{-1} h^{-1} with much

higher NH$_3$ conversion (Figure 6c and Figure S4). Furthermore, it is interesting to note that $Ni_{0.5}Ce_{0.1}Al_{0.4}O_x$ prepared via the AASA route exhibited much higher catalytic activity compared with the catalyst with same composition prepared by the coprecipitation method ($Ni_{0.5}Ce_{0.1}Al_{0.4}O_x$ cp, Figure 6c), confirming the superiority of the AASA approach. Figure S5 shows that the surface areas of cp replicas both exceed 200 m^2 g^{-1}, so the lower catalytic activity of cp replicas cannot be attributed to the factor of low surface area. Such difference in the NH$_3$ conversion of the catalysts with the same compositions may be ascribed to different synthetic procedures. For AASA, the assembly of the microspheres completed within several seconds in gas, while the coprecipitation method included an aging process in solution, which brings differences in interactions of Ni-, Ce-, and Al-species.

As shown in Figure 6d, the tricomponent replica $Ni_{0.5}Ce_{0.1}Al_{0.4}O_x$ exhibited a very high hydrogen formation rate of 109 mmol g^{-1} min^{-1} (at 45 h) during a long-term stability test at 600 °C. This hydrogen formation rate is roughly 4 times that of the reported supported nickel catalyst (Ni/MCM-41 catalyst,[49] 24 mmol g^{-1} min^{-1} at 600 °C), 3 times that of the supported ruthenium catalyst (2 wt % Ru/graphite catalyst,[35] 37 mmol g^{-1} min^{-1} at 450 °C), and 2 times that of the $Ni_{0.5}Ce_{0.1}Al_{0.4}O_x$ cp catalyst (53 mmol g^{-1} min^{-1}). The above results fully prove the superiority on the catalytic performance of the tricomponent $Ni_{0.5}Ce_{0.1}Al_{0.4}O_x$ catalyst, which is both highly efficient and stable for ammonia decomposition. The apparent activation energy (E_{app}) of NH$_3$ decomposition over the catalysts was calculated with the Arrhenius equation from the catalytic data obtained in the kinetics region. As shown in Figure S6, the E_{app} values of $Ni_{0.5}Ce_{0.5}O_x$ (137.1 kJ mol^{-1}), $Ni_{0.5}Al_{0.5}O_x$ (113.5 kJ mol^{-1}), and $Ni_{0.5}Ce_{0.1}Al_{0.4}O_x$ (118.0 kJ mol^{-1}) have little difference, indicating the same reaction pathway in NH$_3$ decomposition
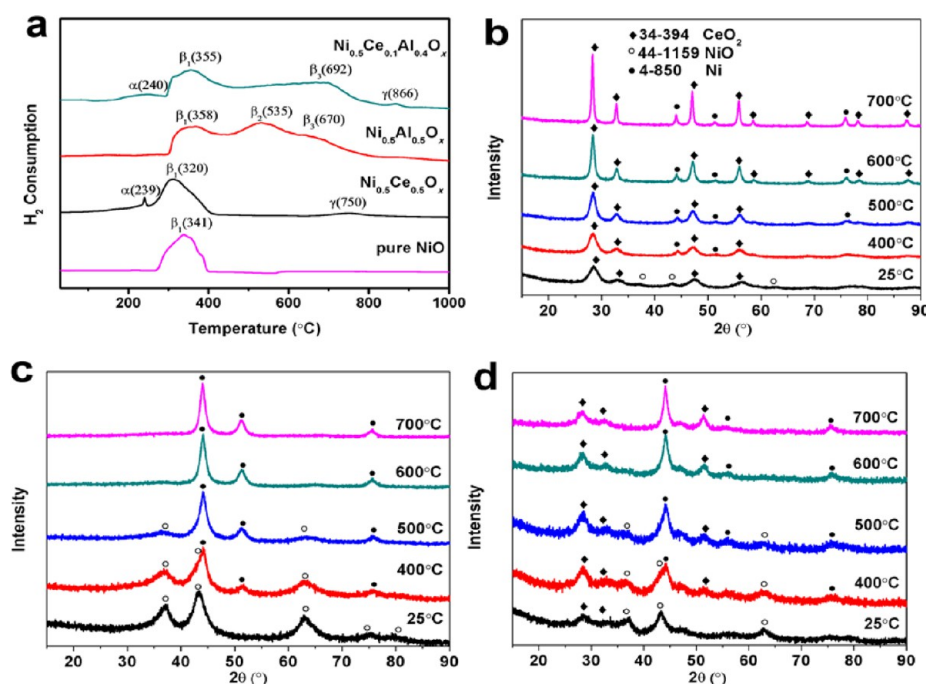
Figure 7. (a) Temperature-programmed reduction by hydrogen (H_2-TPR) profiles over four typical catalysts; (b−d) *in situ* X-ray diffraction (*in situ* XRD) patterns under a similar condition (5% H_2/Ar gas) to that of H_2-TPR measurement of typical replicas produced via AASA. (b) $Ni_{0.5}Ce_{0.5}O_x$; (c) $Ni_{0.5}Al_{0.5}O_x$; (d) $Ni_{0.5}Ce_{0.1}Al_{0.4}O_x$.

for these catalysts. Therefore, the difference in activity and stability among these Ni−Ce−O, Ni−Al−O, and Ni−Ce−Al−O catalysts may come from the textural difference.

XRD patterns of the catalysts after the catalytic tests are shown in Figure 2b and 2c. It is found that diffraction peaks of cubic metallic Ni^0 emerged; meanwhile, rhombohedral nickel oxide was not detected, indicating NiO is reduced to metallic Ni^0 by the generated H_2 during the reaction. The crystal phase of CeO_2 does not change after temperature-dependent catalytic tests, and diffraction peaks of crystallized Al_2O_3 or other Al species are absent. SEM images of replicas after temperature-dependent catalytic tests are displayed in Figure S6. The reduced metallic Ni^0 particles are observed to aggregate on the surface of microspheres. The physical properties of replicas after the stability test with 18000 cm^3 g^{-1} h^{-1} space velocity are listed in Table S1. The sizes of the metallic Ni^0 crystalline domain in each replica were also calculated according to the XRD patterns shown in Figure 2c. Compared to data in Table 1, all tested replicas went through a loss of the surface area, and the aggregation of Ni species led to the size increase of Ni^0 particles.

In order to examine the redox property and interaction between different components, which is related to the activity of the catalyst for NH_3 decomposition, temperature-programmed reduction by hydrogen (H_2-TPR) was carried out over nickel-based mesoporous microsphere products. The TPR profiles corresponding to nickel-based catalysts are depicted in Figure 7a. As can be seen, at the high temperature range of 750−1000 °C, there is a weak reduction peak (γ) for $Ni_{0.5}Ce_{0.5}O_x$ (750 °C) and $Ni_{0.5}Ce_{0.1}Al_{0.4}O_x$ (866 °C), which is ascribed to the reduction of crystalline CeO_2. At low temperatures up to about 240 °C, there is a small and sharp peak for $Ni_{0.5}Ce_{0.5}O_x$ (239 °C) and a weak and broad peak observed on $Ni_{0.5}Ce_{0.1}Al_{0.4}O_x$ (240 °C). We mark this peak as the α peak. According to former reports,[61−63] this reduction

peak (α) is attributed to the reduction of the absorbed surface oxygen, indicating that the introduction of ceria brings in oxygen vacancies for the Ce-containing catalysts. The peaks (β) appearing at temperatures from 300 to 750 °C are related to the reduction of nickel oxide to metallic Ni^0. As for $Ni_{0.5}Ce_{0.5}O_x$, there is only one reduction peak ($\beta1$) centered at 320 °C, which appeared at lower temperature compared to that of the pure NiO sample (at 341 °C), showing that the ceria interacts with nickel oxides, which makes the release of lattice oxygen from nickel oxide more easy and thus promotes its reducibility. The interaction with ceria gives nickel oxide an easier reduction, which means an easier appearance of the active sites, metallic Ni^0. From this point, the ceria−nickel oxide interaction is very likely to enhance the catalytic activities. Three reduction peaks ($\beta1$, $\beta2$, and $\beta3$) were observed from $Ni_{0.5}Al_{0.5}O_x$ at reduction temperatures at 358, 535, and 670 °C. The reduction peak at 358 °C corresponds to the reduction of crystalline NiO ($\beta1$), and the reduction peaks at higher temperatures are attributed to reduction of Ni−O species having weak ($\beta2$) and strong interaction ($\beta3$) with amorphous Al_2O_3.[64,65] For $Ni_{0.5}Ce_{0.1}Al_{0.4}O_x$, the interaction becomes stronger with increasing alumina content, and the reduction peak ($\beta3$) appears at a high temperature (692 °C). According to the data in Table1, we conclude that this strong interaction helps improve the dispersion of nickel oxide and greatly holds back the size increase of metallic Ni^0 during the catalytic process. Based on the above H_2-TPR results, it is clearly shown that the ceria−nickel oxide and alumina−nickel oxide interactions are both closely related to the catalytic activity and stability of the catalyst.

The reduction process was further studied using an *in situ* XRD technique in a 5% H_2/Ar gas mixture under a similar condition to that of H_2-TPR measurement. The corresponding *in situ* XRD patterns are exhibited in Figure 7b to 7d. The temperature region is the same as that of the temperature-

dependent catalytic cycles. As shown in Figure 7b and 7c, the characteristic peaks of metallic Ni^0 appeared at 400 °C for both $Ni_{0.5}Ce_{0.5}O_x$ and $Ni_{0.5}Al_{0.5}O_x$, indicating the reduction is underway. For $Ni_{0.5}Ce_{0.5}O_x$, the characteristic peaks of NiO are absent in any high-temperature tests, which coincides with the H_2-TPR profile, revealing that the reduction of $Ni_{0.5}Ce_{0.5}O_x$ completes at about 400 °C (Figure 7a). Also, the CeO_2 peaks of $Ni_{0.5}Ce_{0.5}O_x$ sharpen when temperature increases, which means CeO_2 nanocrystals in $Ni_{0.5}Ce_{0.5}O_x$ aggregate and grow. However, for $Ni_{0.5}Al_{0.5}O_x$, the characteristic peaks of NiO gradually diminished with temperature increasing and finally vanished at 600 °C. The prolonged reduction process could be explained by the noteworthy interaction between NiO and Al_2O_3, as confirmed by the H_2-TPR results. In Figure 7a, the reduction of $Ni_{0.5}Al_{0.5}O_x$ completes at about 800 °C. The difference in the temperatures of full reduction from *in situ* XRD (600 °C) and H_2-TPR (800 °C) characterizations might be attributed to different heating modes. Furthermore, Figure 7d shows that the CeO_2 peaks of $Ni_{0.5}Ce_{0.1}Al_{0.4}O_x$ are much wider than those of $Ni_{0.5}Ce_{0.5}O_x$, and the other Ni−Ce−Al−O catalyst, such as $Ni_{0.5}Ce_{0.4}Al_{0.1}O_x$, gives the same result (Figure S7a). According to the calculation with the Scherrer equation, as shown in Figure S7b, the crystalline domain size of CeO_2 in $Ni_{0.5}Ce_{0.5}O_x$ is 4.5 nm at 25 °C and 19.8 nm at 700 °C, while that in $Ni_{0.5}Ce_{0.1}Al_{0.4}O_x$ and $Ni_{0.5}Ce_{0.4}Al_{0.1}O_x$ is 4.4 nm at 25 °C and 4.7 nm at 700 °C, 3.5 nm at 25 °C, and 5.4 nm at 700 °C, respectively. This observation denotes that the addition of Al_2O_3 can not only interact with NiO but also stabilize CeO_2, and thus the skeleton of the microsphere is maintained. Hence, the excellent boost in activity of CeO_2 and remarkable stabilization of Al_2O_3 are both essential to the high-performance nickel-based catalysts.

We have mentioned that the crystalline size of the metallic Ni^0 domain is supposed to be the main factor that determines the activity of the catalysts for NH_3 decomposition. For different catalysts, the degrees of reduction could be distinguished by comparing the metallic Ni^0 domain size. For example, as shown in Figure S8 and Figure 8, aggregation of metallic Ni^0 particles could be clearly seen after both a temperature-dependent catalytic test and the long-term stability test at 600 °C (Figure S8a and b, Figure 8a and b), while within
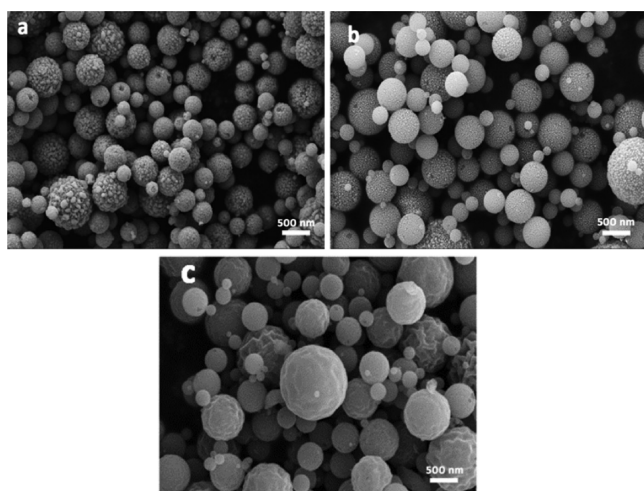

Figure 8. SEM images of typical replicas after long-term stability test at 600 °C: (a) $Ni_{0.5}Ce_{0.5}O_x$; (b) $Ni_{0.5}Al_{0.5}O_x$; (c) $Ni_{0.5}Ce_{0.1}Al_{0.4}O_x$ (GHSV = 18,000 cm^3 g^{-1} h^{-1}).

the selected area aggregation of metallic Ni^0 in $Ni_{0.5}Ce_{0.1}Al_{0.4}O_x$ hardly took place (Figures 8c, S8c, S11, and S12). According to a series of calculations (Table 1 and S1), the metallic Ni^0 in $Ni_{0.5}Ce_{0.5}O_x$ grew from 5.4 nm (fresh replicas) to 16.5 nm after the temperature-dependent catalytic cycles (used replicas), and the average diameter of metallic Ni^0 domains reached 20.5 nm after stability test (AST replicas) of 45 h at 600 °C (Figures 9
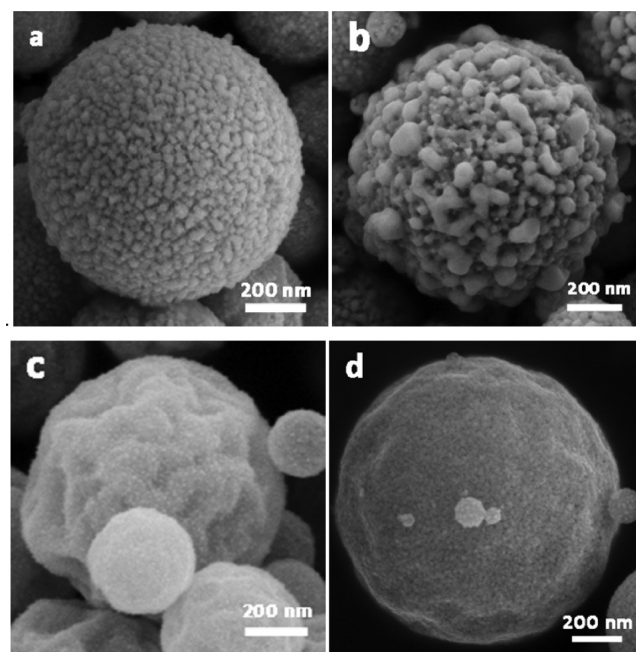
Figure 9. SEM images of $Ni_{0.5}Ce_{0.5}O_x$ (a, b) and $Ni_{0.5}Ce_{0.1}Al_{0.4}O_x$ (c, d) after temperature-dependent catalytic tests (a, c) and after stability test at 600 °C (b, d) (GHSV = 18 000 cm^3 g^{-1} h^{-1}).
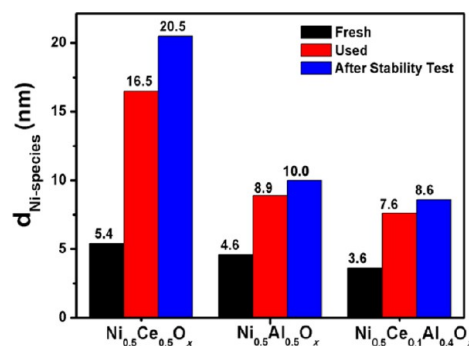
Figure 10. Crystalline domain size of NiO for the multimetal oxide catalysts (calculated from XRD patterns using Scherrer equation) before the temperature-dependent catalytic test and metallic Ni^0 after temperature-dependent catalytic test and stability test (GHSV = 18 000 cm^3 g^{-1} h^{-1}).

and 10). This crystalline size increase also demonstrates the unstable nature of the $Ni_{0.5}Ce_{0.5}O_x$ catalyst. However, when it comes to $Ni_{0.5}Al_{0.5}O_x$, the growth of metallic Ni^0 domains was clearly restricted (4.6, 8.9, and 10.0 nm for fresh, used, and AST replicas, respectively, seen in Figures 9 and 10). This significant difference further proves our conclusion of TPR results, which stresses the importance of the alumina−nickel oxide interaction greatly holding back the reduction process. Besides, considering

the *in situ* XRD characterizations, it was observed that Al_2O_3 also had an interaction with CeO_2, which could prevent the size increase of CeO_2 and keep the homogeneous dispersion of the active sites. Due to the prominent resistance to sintering of the Al_2O_3 component, the loss of surface area for used $Ni_{0.5}Al_{0.5}O_x$ and $Ni_{0.5}Ce_{0.1}Al_{0.4}O$ is also suppressed (Figure S12). The antisintering property allows the Al-containing microspheres to maintain their mesoporous structure to the maximum extent at high temperatures.

It is noticed that, besides the domain size effect of metallic Ni^0, the interaction between CeO_2 and $Ni(II)$ species could play an important role in the activity enhancement of the catalyst. The XANES spectra for the used catalysts after long-term stability tests in Figure 6c exhibit that nickel species in $Ni_{0.5}Al_{0.5}O_x$ were significantly reduced to metallic Ni^0, while nickel in the other samples ($Ni_{0.5}Ce_{0.5}O_x$ and $Ni_{0.5}Ce_{0.1}Al_{0.4}O_x$) was a mixture of metallic Ni^0 and $Ni(II)$ species. The related EXAFS fitting results in Figure 5d and Table 2 identify that for all the used Ce-containing samples, besides the presence of metallic Ni^0, a new shell of Ni–Ni at 2.95–2.98 Å with different coordination numbers from 2.7 to 6.0 was also formed. Compared with the $Ni_{0.5}Al_{0.5}O_x$ sample, some locally disordered Ni–O species that are missing in the XRD patterns (Figure 2b) were examined in the Ce-containing samples using the EXAFS technique, indicating a special interaction between ceria and related nickel species. The enhancement of the activity of the Ce-containing catalysts could come from this interaction.

CONCLUSIONS

In summary, after a case study of Ni–Ce–O, Ni–Al–O, and Ni–Ce–Al–O catalysts for ammonia decomposition, the AASA has been proved to be a dependable way to prepare mesoporous metal oxide materials with tuned compositions. The structural characterizations combining catalytic tests demonstrated the structure–property relationship that metallic Ni^0 is the active site, and the NH_3 conversion declines apparently with the increase of metallic Ni^0 crystalline domain size. The introduction of ceria can greatly enhance the catalytic activity of nickel catalyst at relatively low temperatures due to the strong interaction of nickel oxide and ceria. However, the durability for the Ni–Ce–O system at high temperature in catalysis is poor due to the sintering of both nickel and ceria species under reductive conditions. Meanwhile, the addition of alumina effectively suppressed the growth of both active metallic Ni^0 and ceria promoter in Ni–Ce–Al–O catalyst that both have excellent activity and high stability. Therefore, this work will give inspirations for searching high-performance catalysts among the group of metal oxide materials and also provide a facile approach to potential practical applications.

ASSOCIATED CONTENT

Ⓢ Supporting Information

The Supporting Information is available free of charge on the ACS Publications website at DOI: 10.1021/acs.jpcc.6b01595.

> Physical properties of AST replicas, nitrogen sorption isotherms of some fresh and used replicas, catalytic properties of replicas in each system, Arrhenius plots of catalysts, SEM images and XRD patterns of the used catalysts, and SEM elemental mapping of $Ni_{0.5}Ce_{0.1}Al_{0.4}O_x$ (PDF)

AUTHOR INFORMATION

Corresponding Authors
*E-mail: jinzhao@sdu.edu.cn.
*E-mail: sirui@sinap.ac.cn.
*E-mail: jiacj@sdu.edu.cn.

Notes
The authors declare no competing financial interest.

REFERENCES

(1) Tamiolakis, I.; Lykakis, I. N.; Katsoulidis, A. P.; Stratakis, M.; Armatas, G. M. Mesoporous Cr_2O_3–Phosphomolybdic Acid Solid Solution Frameworks With High Catalytic Activity. *Chem. Mater.* **2011**, *23*, 4204–4211.

(2) Zhu, H.; Zhao, J.; Liu, J.; Yang, X.; Shen, Y. General Synthesis of a Mesoporous Composite of Metal Oxide and Silicate Nanoparticles from a Metal Salt and Laponite Suspension for Catalysis. *Chem. Mater.* **2006**, *18*, 3993–4001.

(3) Grewe, T.; Deng, H.; Weidenthaler, C.; Schüth, F.; Tüysüz, H. Design of Ordered Mesoporous Composite Materials and Their Electrocatalytic Activities for Water Oxidation. *Chem. Mater.* **2013**, *25*, 4926–4935.

(4) Noda, Y.; Lee, B.; Domen, K.; Kondo, J. N. Synthesis of Crystallized Mesoporous Tantalum Oxide and Its Photocatalytic Activity for Overall Water Splitting under Ultraviolet Light Irradiation. *Chem. Mater.* **2008**, *20*, 5361–5367.

(5) Kondo, J. N.; Uchida, M.; Nakajima, K.; Lu, D.; Hara, M.; Domen, K. Synthesis, Mesostructure, and Photocatalysis of a Highly Ordered and Thermally Stable Mesoporous Mg and Ta Mixed Oxide. *Chem. Mater.* **2004**, *16*, 4304–4310.

(6) Cai, W.; Yu, J.; Anand, C.; Vinu, A.; Jaroniec, M. Facile Synthesis of Ordered Mesoporous Alumina and Alumina-Supported Metal Oxides with Tailored Adsorption and Framework Properties. *Chem. Mater.* **2011**, *23*, 1147–1157.

(7) Weidmann, C.; Brezesinski, K.; Suchomski, C.; Tropp, K.; Grosser, N.; Haetge, J.; Smarsly, B. M.; Brezesinski, T. Morphology-Controlled Synthesis of Nanocrystalline η-Al_2O_3 Thin Films, Powders, Microbeads, and Nanofibers with Tunable Pore Sizes from Preformed Oligomeric Oxo-Hydroxo Building Blocks. *Chem. Mater.* **2012**, *24*, 486–494.

(8) Kay, A.; Grätzel, M. Dye-Sensitized Core–Shell Nanocrystals: Improved Efficiency of Mesoporous Tin Oxide Electrodes Coated with a Thin Layer of an Insulating Oxide. *Chem. Mater.* **2002**, *14*, 2930–2935.

(9) Chen, Y.; Chen, H.; Zeng, D.; Tian, Y.; Chen, F.; Feng, J.; Shi, J. Core/Shell Structured Hollow Mesoporous Nanocapsules: A Potential Platform for Simultaneous Cell Imaging and Anticancer Drug Delivery. *ACS Nano* **2010**, *4*, 6001–6013.

(10) Julián-López, B.; Boissiére, C. d.; Chanéac, C.; Grosso, D.; Vasseur, S.; Miraux, S.; Duguet, E.; Sanchez, C. M. Mesoporous Maghemite–organosilica Microspheres: A Promising Route Towards

Multifunctional Platforms for Smart Diagnosis and Therapy. *J. Mater. Chem.* **2007**, *17*, 1563.

(11) Chen, Y.; Chen, H.; Zhang, S.; Chen, F.; Zhang, L.; Zhang, J.; Zhu, M.; Wu, H.; Guo, L.; Feng, J.; Shi, J. Multifunctional Mesoporous Nanoellipsoids for Biological Bimodal Imaging and Magnetically Targeted Delivery of Anticancer Drugs. *Adv. Funct. Mater.* **2011**, *21*, 270−278.

(12) Kim, J.; Kim, H. S.; Lee, N.; Kim, T.; Kim, H.; Yu, T.; Song, I. C.; Moon, W. K.; Hyeon, T. Multifunctional Uniform Nanoparticles Composed of a Magnetite Nanocrystal Core and a Mesoporous Silica Shell for Magnetic Resonance and Fluorescence Imaging and for Drug Delivery. *Angew. Chem., Int. Ed.* **2008**, *47*, 8438−8441.

(13) Lee, J. E.; Lee, N.; Kim, H.; Kim, J.; Choi, S. H.; Kim, J. H.; Kim, T.; Song, I. C.; Park, S. P.; Moon, W. K.; et al. Uniform Mesoporous Dye-Doped Silica Nanoparticles Decorated with Multiple Magnetite Nanocrystals for Simultaneous Enhanced Magnetic Resonance Imaging, Fluorescence Imaging, and Drug Delivery. *J. Am. Chem. Soc.* **2009**, *132*, 552−557.

(14) Antonelli, D. M.; Ying, J. Y. Synthesis of Hexagonally Packed Mesoporous TiO$_2$ by a Modified Sol−gel Method. *Angew. Chem., Int. Ed. Engl.* **1995**, *34*, 2014−2017.

(15) Soler-Illia, G. J. d. A.; Sanchez, C.; Lebeau, B.; Patarin, J. Chemical Strategies To Design Textured Materials: from Microporous and Mesoporous Oxides to Nanonetworks and Hierarchical Structures. *Chem. Rev.* **2002**, *102*, 4093−4138.

(16) Gu, D.; Schüth, F. Synthesis of Non-siliceous Mesoporous Oxides. *Chem. Soc. Rev.* **2014**, *43*, 313−344.

(17) Lu, Y.; Fan, H.; Stump, A.; Ward, T. L.; Rieker, T.; Brinker, C. J. Aerosol-assisted Self-assembly of Mesostructured Spherical Nano-particles. *Nature* **1999**, *398*, 223−226.

(18) Brinker, C. J.; Lu, Y.; Sellinger, A.; Fan, H. Evaporation-Induced Self-Assembly: Nanostructures Made Easy. *Adv. Mater.* **1999**, *11*, 579−585.

(19) Lu, Y.; Fan, H.; Doke, N.; Loy, D. A.; Assink, R. A.; LaVan, D. A.; Brinker, C. J. Evaporation-Induced Self-Assembly of Hybrid Bridged Silsesquioxane Film and Particulate Mesophases with Integral Organic Functionality. *J. Am. Chem. Soc.* **2000**, *122*, 5258−5261.

(20) Jiang, X.; Brinker, C. J. Aerosol-assisted Self-assembly of Single-crystal Core/Nanoporous Shell Particles as Model Controlled Release Capsules. *J. Am. Chem. Soc.* **2006**, *128*, 4512−4513.

(21) Li, L.; Tsung, C.-K.; Ming, T.; Sun, Z.; Ni, W.; Shi, Q.; Stucky, G. D.; Wang, J. Multifunctional Mesostructured Silica Microspheres from an Ultrasonic Aerosol Spray. *Adv. Funct. Mater.* **2008**, *18*, 2956−2962.

(22) Tsung, C. K.; Fan, J.; Zheng, N.; Shi, Q.; Forman, A. J.; Wang, J.; Stucky, G. D. A General Route to Diverse Mesoporous Metal Oxide Submicrospheres with Highly Crystalline Frameworks. *Angew. Chem., Int. Ed.* **2008**, *47*, 8682−8686.

(23) Jin, Z.; Xiao, M.; Bao, Z.; Wang, P.; Wang, J. A General Approach to Mesoporous Metal Oxide Microspheres Loaded with Noble Metal Nanoparticles. *Angew. Chem., Int. Ed.* **2012**, *51*, 6406−6410.

(24) Jin, Z.; Wang, F.; Wang, F.; Wang, J.; Yu, J. C.; Wang, J. Metal Nanocrystal-Embedded Hollow Mesoporous TiO$_2$ and ZrO$_2$ Micro-spheres Prepared with Polystyrene Nanospheres as Carriers and Templates. *Adv. Funct. Mater.* **2013**, *23*, 2137−2144.

(25) Kuai, L.; Geng, J.; Chen, C.; Kan, E.; Liu, Y.; Wang, Q.; Geng, B. A Reliable Aerosol-Spray-Assisted Approach to Produce and Optimize Amorphous Metal Oxide Catalysts for Electrochemical Water Splitting. *Angew. Chem., Int. Ed.* **2014**, *53*, 7547−7451.

(26) Kuai, L.; Wang, J.; Ming, T.; Fang, C.; Sun, Z.; Geng, B.; Wang, J. Aerosol-spray Diverse Mesoporous Metal Oxides from Metal Nitrates. *Sci. Rep.* **2015**, *5*, 9923.

(27) Schüth, F.; Palkovits, R.; Schlögl, R.; Su, D. S. Ammonia as a Possible Element in an Energy Infrastructure: Catalysts for Ammonia Decomposition. *Energy Environ. Sci.* **2012**, *5*, 6278−6289.

(28) Yin, S. F.; Xu, B. Q.; Zhou, X. P.; Au, C. T. A Mini-review on Ammonia Decomposition Catalysts for On-site Generation of Hydrogen for Fuel Cell Applications. *Appl. Catal., A* **2004**, *277*, 1−9.

(29) Raróg, W.; Kowalczyk, Z.; Sentek, J.; Składanowski, D.; Zieliński, J. Effect of K, Cs and Ba on the Kinetics of NH$_3$ Synthesis over Carbon-based Ruthenium Catalysts. *Catal. Lett.* **2000**, *68*, 163−168.

(30) Kowalczyk, Z.; Sentek, J.; Jodzis, S.; Muhler, M.; Hinrichsen, O. Effect of Potassium on the Kinetics of Ammonia Synthesis and Decomposition over Fused Iron Catalyst at Atmospheric Pressure. *J. Catal.* **1997**, *169*, 407−414.

(31) Boisen, A.; Dahl, S.; Nørskov, J. K.; Christensen, C. H. Why the Optimal Ammonia Synthesis Catalyst Is Not the Optimal Ammonia Decomposition Catalyst. *J. Catal.* **2005**, *230*, 309−312.

(32) Arabczyk, W.; Zamlynny, J. Study of the Ammonia Decomposition over Iron Catalysts. *Catal. Lett.* **1999**, *60*, 167−171.

(33) Yin, S.-F.; Zhang, Q.-H.; Xu, B.-Q.; Zhu, W.-X.; Ng, C.-F.; Au, C.-T. Investigation on the Catalysis of CO$_x$-free Hydrogen Generation from Ammonia. *J. Catal.* **2004**, *224*, 384−396.

(34) Rarogpilecka, W.; Miskiewicz, E.; Szmigiel, D.; Kowalczyk, Z. Structure Sensitivity of Ammonia Synthesis over Promoted Ruthenium Catalysts Supported on Graphitised Carbon. *J. Catal.* **2005**, *231*, 11−19.

(35) Zheng, W.; Cotter, T. P.; Kaghazchi, P.; Jacob, T.; Frank, B.; Schlichte, K.; Zhang, W.; Su, D. S.; Schüth, F.; Schlögl, R. Experimental and Theoretical Investigation of Molybdenum Carbide and Nitride as Catalysts for Ammonia Decomposition. *J. Am. Chem. Soc.* **2013**, *135*, 3458−3464.

(36) Leewis, C. M.; Kessels, W. M. M.; Sanden, M. C. M. v. d.; Niemantsverdriet, J. W. Ammonia Adsorption and Decomposition on Silica Supported Rh Nanoparticles Observed by In situ Attenuated Total Reflection Infrared Spectroscopy. *Appl. Surf. Sci.* **2006**, *253*, 572−580.

(37) Chmielarz, L.; Jabłońska, M.; Strumiński, A.; Piwowarska, Z.; Węgrzyn, A.; Witkowski, S.; Michalik, M. Selective Catalytic Oxidation of Ammonia to Nitrogen over Mg-Al, Cu-Mg-Al and Fe-Mg-Al Mixed Metal Oxides Doped with Noble Metals. *Appl. Catal., B* **2013**, *130−131*, 152−162.

(38) Chen, W.; Ermanoski, I.; Madey, T. E. Decomposition of Ammonia and Hydrogen on Ir Surfaces: Structure Sensitivity and Nanometer-Scale Size Effects. *J. Am. Chem. Soc.* **2005**, *127*, 5014−5015.

(39) Garcia-Garcia, F. R.; Guerrero-Ruiz, A.; Rodriguez-Ramos, I.; Goguet, A.; Shekhtman, S. O.; Hardacre, C. TAP Studies of Ammonia Decomposition over Ru and Ir Catalysts. *Phys. Chem. Chem. Phys.* **2011**, *13*, 12892−12899.

(40) Brunauer, S.; Love, K. S.; Keenan, R. G. Adsorption of Nitrogen and the Mechanism of Ammonia Decomposition Over Iron Catalysts. *J. Am. Chem. Soc.* **1942**, *64*, 751−758.

(41) Guo, J.; Wang, P.; Wu, G.; Wu, A.; Hu, D.; Xiong, Z.; Wang, J.; Yu, P.; Chang, F.; Chen, Z.; Cheng, P.; et al. Lithium Imide Synergy with 3d Transition-Metal Nitrides Leading to Unprecedented Catalytic Activities for Ammonia Decomposition. *Angew. Chem., Int. Ed.* **2015**, *54*, 2950−2954.

(42) Zhang, J.; Comotti, M.; Schüth, F.; Schlögl, R.; Su, D. S. Commercial Fe- or Co-Containing Carbon Nanotubes as Catalysts for NH$_3$ Decomposition. *Chem. Commun.* **2007**, 1916−1918.

(43) Tagliazucca, V.; Schlichte, K.; Schüth, F.; Weidenthaler, C. Molybdenum-based Catalysts for the Decomposition of Ammonia: In situ X-ray Diffraction Studies, Microstructure, and Catalytic Properties. *J. Catal.* **2013**, *305*, 277−289.

(44) Gu, Y.; Fu, X.; Du, P.; Gu, D.; Jin, Z.; Huang, Y.; Si, R.; Zheng, L.; Song, Q.; Jia, C.; Weidenthaler, C. In Situ X-ray Diffraction Study of Co−Al Nanocomposites as Catalysts for Ammonia Decomposition. *J. Phys. Chem. C* **2015**, *119*, 17102−17110.

(45) Zhang, J.; Xu, H.; Jin, X.; Ge, Q.; Li, W. Characterizations and Activities of the Nano-sized Ni/Al$_2$O$_3$ and Ni/La−Al$_2$O$_3$ Catalysts for NH$_3$ Decomposition. *Appl. Catal., A* **2005**, *290*, 87−96.

(46) Gu, Y.; Jin, Z.; Zhang, H.; Xu, R.; Zheng, M.; Guo, Y.; Song, Q.; Jia, C. Transition Metal Nanoparticles Dispersed in an Alumina Matrix as Active and Stable Catalysts for CO$_x$-free Hydrogen Production from Ammonia. *J. Mater. Chem. A* **2015**, *3*, 17172−17180.

(47) Liu, H.; Wang, H.; Shen, J.; Sun, Y.; Liu, Z. Preparation, Characterization and Activities of the Nano-sized Ni/SBA-15 Catalyst for Producing CO_x-free Hydrogen from Ammonia. *Appl. Catal., A* **2008**, *337*, 138−147.

(48) Zheng, W.; Zhang, J.; Ge, Q.; Xu, H.; Li, W. Effects of CeO_2 Addition on Ni/Al_2O_3 Catalysts for the Reaction of Ammonia Decomposition to Hydrogen. *Appl. Catal., B* **2008**, *80*, 98−105.

(49) Li, X.; Ji, W.; Zhao, J.; Wang, S.; Au, C. Ammonia Decomposition over Ru and Ni Catalysts Supported on Fumed SiO_2, MCM-41, and SBA-15. *J. Catal.* **2005**, *236*, 181−189.

(50) Choudhary, T. V.; Sivadinarayana, C.; Goodman, D. W. Catalytic Ammonia Decomposition: COx-free Hydrogen Production for Fuel Cell Applications. *Catal. Lett.* **2001**, *72*, 197−201.

(51) Lu, A.; Nitz, J.; Comotti, M.; Weidenthaler, C.; Schlichte, K.; Lehmann, C. W.; Terasaki, O.; Schüth, F. Spatially and Size Selective Synthesis of Fe-Based Nanoparticles on Ordered Mesoporous Supports as Highly Active and Stable Catalysts for Ammonia Decomposition. *J. Am. Chem. Soc.* **2010**, *132*, 14152−14162.

(52) Liu, H.; Wang, H.; Shen, J.; Sun, Y.; Liu, Z. Promotion Effect of Cerium and Lanthanum Oxides on Ni/SBA-15 Catalyst for Ammonia Decomposition. *Catal. Today* **2008**, *131*, 444−449.

(53) Lenggoro, I. W.; Hata, T.; Iskandar, F.; Lunden, M. M.; Okuyama, K. An Experimental and Modeling Investigation of Particle Production by Spray Pyrolysis Using a Laminar Flow Aerosol Reactor. *J. Mater. Res.* **2000**, *15*, 733−743.

(54) Grosvenor, A. P.; Biesinger, M. C.; Smart, R. S. C.; McIntyre, N. S. New Interpretations of XPS Spectra of Nickel Metal and Oxides. *Surf. Sci.* **2006**, *600*, 1771−1779.

(55) Bianchi, C. L.; Cattania, M. G.; Villa, P. XPS Characterization of Ni and Mo Oxides Before and After "In situ" Treatments. *Appl. Surf. Sci.* **1993**, *70*, 211−216.

(56) Mullins, D.; Overbury, S.; Huntley, D. Electron Spectroscopy of Single Crystal and Polycrystalline Cerium Oxide Surfaces. *Surf. Sci.* **1998**, *409*, 307−319.

(57) Grunze, M.; Golze, M.; Driscoll, R.; Dowben, P. Ammonia Adsorption and Decomposition on a Ni(110) Surface. *J. Vac. Sci. Technol.* **1981**, *18*, 611−615.

(58) Seabury, C.; Rhodin, T.; Purtell, R.; Merrill, R. Chemisorption and Reaction of NH_3 on Ni(111). *Surf. Sci.* **1980**, *93*, 117−126.

(59) Liang, C.; Li, W.; Wei, Z.; Xin, Q.; Li, C. Catalytic Decomposition of Ammonia over Nitrided MoNx/α-Al_2O_3 and NiMoNy/α-Al_2O_3 Catalysts. *Ind. Eng. Chem. Res.* **2000**, *39*, 3694−3697.

(60) Zhuang, Q.; Qin, Y.; Chang, L. Promoting Effect of Cerium Oxide in Supported Nickel Catalyst for Hydrocarbon Steam-reforming. *Appl. Catal.* **1991**, *70*, 1−8.

(61) Shan, W.; Luo, M.; Ying, P.; Shen, W.; Li, C. Reduction Property and Catalytic Activity of Ce_1−XNi$_X$$O_2$ Mixed Oxide Catalysts for CH_4 Oxidation. *Appl. Catal., A* **2003**, *246*, 1−9.

(62) Zhang, B.; Tang, X.; Li, Y.; Cai, W.; Xu, Y.; Shen, W. Steam Reforming of Bio-ethanol for the Production of Hydrogen over Ceria-supported Co, Ir and Ni Catalysts. *Catal. Commun.* **2006**, *7*, 367−372.

(63) Zhang, C.; Li, S.; Wu, G.; Gong, J. Synthesis of Stable Ni-CeO_2 Catalysts via Ball-milling for Ethanol Steam Reforming. *Catal. Today* **2014**, *233*, 53−60.

(64) Roh, H.-S.; Jun, K.-W. Carbon Dioxide Reforming of Methane over Ni Catalysts Supported on Al_2O_3 Modified with La_2O_3, MgO, and CaO. *Catal. Surv. Asia* **2008**, *12*, 239−252.

(65) Alipour, Z.; Rezaei, M.; Meshkani, F. Effects of Support Modifiers on the Catalytic Performance of Ni/Al_2O_3 Catalyst in CO_2 Reforming of Methane. *Fuel* **2014**, *129*, 197−203.